The expansion of a collisionless plasma into a plasma of lower density

M. Perego, P. D. Howell, M. D. Gunzburger, J. R. Ockendon, and J. E. Allen

Citation: Physics of Plasmas **20**, 052101 (2013); doi: 10.1063/1.4802933
View online: http://dx.doi.org/10.1063/1.4802933
View Table of Contents: http://scitation.aip.org/content/aip/journal/pop/20/5?ver=pdfcov
Published by the AIP Publishing

The expansion of a collisionless plasma into a plasma of lower density

M. Perego,[1] P. D. Howell,[2] M. D. Gunzburger,[1] J. R. Ockendon,[2] and J. E. Allen[2]
[1]*Department of Scientific Computing, Florida State University, Tallahassee, Florida 32306, USA*
[2]*OCIAM, Mathematical Institute, Oxford University, 24-29 St Giles, OX1 3LB Oxford, United Kingdom*

(Received 12 March 2013; accepted 9 April 2013; published online 2 May 2013)

This paper considers the asymptotic and numerical solution of a simple model for the expansion of a collisionless plasma into a plasma of lower density. The dependence on the density ratio of qualitative and quantitative features of solutions of the well-known cold-ion model is explored. In the cold-ion limit, we find that a singularity develops in the ion density in finite time unless the density ratio is zero or close to unity. The classical cold-ion model may cease to be valid when such a singularity occurs and we then regularize the model by the finite ion-temperature Vlasov-Poisson system. Numerical evidence suggests the emergence of a multi-modal velocity distribution. © *2013 AIP Publishing LLC*. [http://dx.doi.org/10.1063/1.4802933]

I. INTRODUCTION

The expansion of a collision-free plasma into a vacuum was studied mathematically in Ref. 1, under the assumption of quasi-neutrality, a concept pioneered in Ref. 2. In Ref. 3, this assumption was relaxed to include space charge, modelled by the Poisson equation. As in Ref. 1, it was assumed that the electron density is given by the Boltzmann relation, but the thermal energy of the positive ions was neglected in comparison with the electron thermal energy. The Boltzmann assumption is valid as long as the electron thermal speed greatly exceeds the ion velocity, which is valid in the early stages of the expansion. Another requirement was that the plasma should be large enough for boundary effects to be neglected. The acceleration of positive ions to high energies was predicted in Ref. 3 where it was indicated that possible fields of application were solar flares and the emission of high-energy ions by laser-produced plasmas of medium density. The latter prediction proved to be true, and an example is given in Ref. 4. References to other relevant experiments can be found in Ref. 5, which deals with the same problem as that of Ref. 3. However, a different numerical method, based on a Lagrangian formulation, was used and it predicted different behavior near the ion front.

A central goal of the present paper is to gain further insights into the expansion of a collisionless plasma into a plasma of lower density; phenomena of this kind are to be found both in the laboratory and in space. Initially, as in the previous studies cited above, we adopt the well-known cold-ion model (see Refs. 3 and 5). We provide extensive analytical and computational results demonstrating that expansion into a lower density plasma may differ profoundly from expansion into a vacuum. In particular, we find that the expanding front is preceded by a train of ion-acoustic waves and that the solution may develop a finite-time "spike", with the ion density apparently tending to infinity. These observations are confirmed by detailed asymptotic analyses of the cold-ion equations.

A related problem was studied in Ref. 6, where expansion into a vacuum was considered but with an exponentially smooth front rather than a sharp front, and the resulting model was solved numerically using a particle method. The formation of spikes in the ion density was observed, as in the present paper, and identified with a "wave-breaking" phenomenon, following which the ion velocity becomes a multi-valued function of position. Qualitatively similar behaviour was observed in Ref. 7 using a simplified model in which the electrons were neglected.

The assumption of "cold ions" clearly represents a serious limitation to the above theories. As pointed out in Ref. 6, when the ion velocity becomes multi-valued, the cold-ion description is no longer valid, and it must be questioned whether the subsequent behaviour is a good model for the behaviour of thermal ions when the temperature is small but nonzero. The present paper addresses this question by solving numerically the finite-temperature Vlasov-Poisson model for the distribution of ions. We find that solutions of the Vlasov-Poisson model converge to those of the cold-ion model as the ion temperature tends to zero provided the initial jump in the ion density is sufficiently small. Otherwise, following the formation of a spike in the ion density, the solutions of the two models disagree both qualitatively and quantitatively.

Our work is a generalization of that in Refs. 3 and 5; there, further assumptions are made that the ions are cold and that the expansion is into a vacuum. By relaxing these assumptions, we are able to study not only the dramatic effects of wave dispersion but also the way in which the Vlasov-Poisson model is a regularization of the cold-ion model in both the nonlinear and linear regimes, the latter corresponding to a small density change across $x = 0$ at $t = 0$.

We consider only the simplest Vlasov-Poisson model for the distribution function $f_i(x, \mathrm{v}, t)$ of singly charged ions and assume that the electrons, whose thermal velocity greatly exceeds their drift velocity, are everywhere in thermodynamic equilibrium. Thus, the electron density n_e is given by the Boltzmann relation

$$n_e = n_0 \exp\left(\frac{eV}{k T_e}\right), \tag{1}$$

where, in the usual notation, V denotes the electric potential and n_0 a constant reference density.

Using, where appropriate, the notation of Ref. 3, our dimensional model comprises of the Vlasov equation

$$\frac{\partial f_i}{\partial t} + \mathrm{v}\frac{\partial f_i}{\partial x} - \frac{e}{M}\frac{\partial V}{\partial x}\frac{\partial f_i}{\partial \mathrm{v}} = 0, \tag{2}$$

where v denotes the ion velocity in the x-direction, transverse velocity fluctuations having been factored out, and the Poisson equation

$$\varepsilon_0 \frac{\partial^2 V}{\partial x^2} = e(n_e - n_i), \tag{3}$$

where

$$n_i(x,t) = \int_{-\infty}^{\infty} f_i(x,\mathrm{v},t)d\mathrm{v}. \tag{4}$$

The Poisson equation is valid because the velocities in the problem are much smaller than the velocity of light, so that a quasistatic approximation can be employed.

The systems (1)–(4) are solved in $-\infty < x < \infty$ subject to the initial conditions that the ions are in equilibrium with zero drift velocity, so that

$$f_i(x,\mathrm{v},0) = n_i(x,0)\left(\frac{M}{2\pi k T_i}\right)^{\frac{1}{2}} \exp\left(-\frac{M\mathrm{v}^2}{2kT_i}\right) \tag{5}$$

and $n_i(x,0)$ takes the constant values n_0 in $x<0$ and $n_r n_0$ in $x>0$, with $n_r \in [0,1)$. Thus, n_r is simply the ratio of the constant densities in the initial low and high density regions. This prescription of n_i allows V to be calculated at $t=0$ from the numerical integration of (3) subject to the conditions that $\frac{\partial V}{\partial x} \to 0$ as $x \to \pm\infty$; these asymptotic conditions apply throughout the expansion process. Notice that, because of (3), the plasma remains electrically neutral as $x \to \pm\infty$ and hence $n_e(-\infty,t) = n_i(-\infty,t) = n_0$ and $n_e(+\infty,t) = n_i(+\infty,t) = n_r n_0$.

In the cold-ion limit, (5) is replaced by

$$f_i(x,\mathrm{v},0) = n_i(x,0)\,\delta(\mathrm{v}).$$

The cold-ion system can be formally derived assuming that for any $t \geq 0, f_i$ has the form

$$f_i(x,\mathrm{v},t) = n_i(x,t)\,\delta(\mathrm{v} - v_i(x,t)),$$

where v_i is given by

$$v_i = \frac{1}{n_i}\int_{-\infty}^{\infty} \mathrm{v} f_i d\mathrm{v} \quad \text{when} \quad n_i \neq 0.$$

Equation (2) can be integrated with respect to v to yield the conservation law

$$\frac{\partial n_i}{\partial t} + \frac{\partial}{\partial x}(n_i v_i) = 0. \tag{6}$$

Although (6) holds even when $T_i > 0$, it is only in the cold-ion case that the system can be closed via the v-integral of the first moment of (2), which yields the ion-momentum equation

$$\frac{\partial(n_i v_i)}{\partial t} + \frac{\partial(n_i v_i^2)}{\partial x} = -\frac{e}{M} n_i \frac{\partial V}{\partial x}. \tag{7}$$

Coupling (6) with (7), we obtain, for smooth functions n_i and v_i, $n_i \neq 0$,

$$\frac{\partial v_i}{\partial t} + v_i \frac{\partial v_i}{\partial x} = -\frac{e}{M}\frac{\partial V}{\partial x}. \tag{8}$$

The system (1), (3), (6), and (8) defines the cold-ion model for the macroscopic variables n_i, v_i, n_e, and V as used in the computations in Ref. 3.

For analytic convenience, we normalize the variables according to the non-dimensionalizations given in Table I, which leads to the dimensionless Vlasov-Poisson model

$$\frac{\partial f}{\partial t} + \mathrm{v}\frac{\partial f}{\partial x} - \frac{\partial \phi}{\partial x}\frac{\partial f}{\partial \mathrm{v}} = 0, \tag{9}$$

$$\frac{\partial^2 \phi}{\partial x^2} = \exp(\phi) - n, \tag{10}$$

$$n = \int_{-\infty}^{\infty} f d\mathrm{v}, \tag{11}$$

$$n(x,0) = \begin{cases} 1 & x < 1 \\ n_r & x > 0, \end{cases} \tag{12}$$

and

$$f(x,\mathrm{v},0) = n(x,0)\frac{1}{\sqrt{2\pi}\,\varepsilon}\exp\left(-\frac{\mathrm{v}^2}{2\varepsilon^2}\right), \tag{13}$$

where $\varepsilon = \sqrt{T_i/T_e}$ is the key dimensionless parameter measuring the ion temperature. The dimensionless electric field is given by $E = -\partial\phi/\partial x$.

As $\varepsilon \to 0$, one expects to retrieve the well-known cold-ion limit system, which in dimensionless form is

$$\frac{\partial n}{\partial t} + \frac{\partial}{\partial x}(nv) = 0, \quad \frac{\partial v}{\partial t} + v\frac{\partial v}{\partial x} = -\frac{\partial \phi}{\partial x}, \tag{14}$$

together with (10), where the dimensionless cold-ion velocity v is defined by

$$v = \frac{1}{n}\int_{-\infty}^{\infty} \mathrm{v} f d\mathrm{v}; \tag{15}$$

the initial conditions are given by (12), and from (15), $v(x,0) = 0$ where $n(x,0) > 0$. However, we will find that this expectation is not fulfilled in many cases. Indeed, the model (10), (14) may fail completely.

In Secs. II and III, we consider solutions of the cold-ion model with the aim of understanding how the ion oscillations that occur in the expansion depend on n_r. In particular, as $n_r \uparrow 1$, we expect the solution to involve ion-acoustic waves, which are the linearization of (10) and (14) about $n=1$,

TABLE I. Dimensional and dimensionless variables and the reference values used for the non-dimensionalizations; the ← symbol indicates that the dimensionless variable is given the same symbol as its dimensional parent.

Variable		
Dimensional	Dimensionless	Reference value used for Non-dimensionalization
n_i	$n := \frac{n_i}{n_0}$	n_0
n_e	$n_e \leftarrow \frac{n_e}{n_0}$	n_0
x	$x \leftarrow \frac{x}{\lambda_d}$	Electron Debye distance $\lambda_d := \left(\frac{\varepsilon_0 k T_e}{n_0 e^2}\right)^{1/2}$
v	$\mathrm{v} \leftarrow \frac{\mathrm{v}}{c_s}$	ion acoustic speed $c_s := \left(\frac{kT_e}{M}\right)^{\frac{1}{2}}$
v_i	$v := \frac{v_i}{c_s}$	c_s
V	$\phi := \frac{eV}{kT_e}$	$\frac{kT_e}{e}$
t	$t \leftarrow \frac{t}{\omega_{pi}^{-1}}$	reciprocal of the ion plasma frequency $\omega_{pi}^{-1} := \left(\frac{\varepsilon_0 M}{n_0 e^2}\right)^{\frac{1}{2}}$
f_i	$f := \frac{c_s f_i}{n_0}$	$n_0 c_s^{-1}$

$\phi = 0$, and $v = 0$. In Sec. III A, we will see that these waves are described by the well-known dispersion relation (see Ref. 8)

$$\omega^2 = \frac{k^2}{1+k^2}, \tag{16}$$

so we expect strong dispersive effects in this case.

The numerical predictions in Sec. II strongly suggest the possibility of finite-time blow up when the expansion is nonlinear and further evidence concerning the "spikes" that appear in n is given in the computational results in Sec. III.

In Sec. IV, we revert to the model with $T_i > 0$, i.e., the Vlasov-Poisson model (9)–(13), for which we expect Landau damping to accompany dispersion. Although nonlinear Landau damping has recently been studied in Ref. 9, analytical formulae for damping coefficients only exist in the linear case. As suggested in Refs. 10 and 11, the damping rate is exponentially small in T_i.

II. THE COLD-ION MODEL

A. Mathematical classification

We write the system (14) as

$$\frac{\partial \mathbf{u}}{\partial t} + \frac{\partial}{\partial x}\mathbf{f}(\mathbf{u}) = 0, \tag{17}$$

where $\mathbf{u}$ and $\mathbf{f}$ are defined as

$$\mathbf{u} = \begin{bmatrix} n \\ v \end{bmatrix} \quad \mathbf{f}(\mathbf{u}) = \begin{bmatrix} n\,v \\ \frac{1}{2}v^2 + \phi \end{bmatrix}.$$

Note that $\mathbf{f}$ is not a simple function of $\mathbf{u}$ but is an integro-differential operator because ϕ is a functional of n obtained by solving the Poisson equation (10). For this reason, (17) cannot be considered as a traditional hyperbolic system. However, it is useful to analyze the problem by computing the Jacobian of $\mathbf{f}$ and examining its eigenvalues and eigenvectors. The Jacobian of $\mathbf{f}$ is given by

$$J(\mathbf{u}) = \begin{bmatrix} v & n \\ D\phi & v \end{bmatrix},$$

where $D\phi$ is the Gateaux derivative of ϕ with respect to n. We denote by φ_n the Gateaux derivative ϕ with respect to n in the direction n, namely $\varphi_n = \langle D\phi(n), n\rangle$. The Jacobian of $\mathbf{f}$ has eigenvalues $\lambda^{\pm}$ and eigenvectors $\mathbf{u}^{\pm}$ given by

$$\lambda^{\pm} = v \pm \sqrt{\varphi_n} \quad \text{and} \quad \mathbf{u}^{\pm} = \begin{bmatrix} n \\ \pm\sqrt{\varphi_n} \end{bmatrix}.$$

It follows that the linearized system admits two characteristic waves propagating with velocities λ^+ and λ^-. As will be seen in our simulations, λ^+ is positive all over the domain (v is non-negative), whereas λ^- can be negative. Also, for $n_r > 0$, $\lambda^{\pm} = \pm 1$ as $x \to \pm\infty$.

B. The quasi-neutral model

A simplification of the cold-ion model, referred to as the *quasi-neutral model* (see Ref. 12), is obtained by neglecting the left-hand side of the Poisson equation (10), thus obtaining $\phi = \ln(n)$. This model is motivated by the fact that far from the front, the derivative of the potential ϕ is close to zero. The resulting equations are the well-known equations of isothermal gas dynamics. In this case, the eigenvalues of the hyperbolic system are $\lambda^{\pm} = v \pm 1$, and the self-similar solution is given by

$$[n,v]^T = \begin{cases} [1,0]^T & \text{if } x \le t \\ \left[\exp\left(-\frac{x}{t}-1\right), \frac{x}{t}+1\right]^T & \text{if } t < x \le (v_m - 1)t \\ [\exp(-v_m), v_m]^T & \text{if } (v_m-1)t \le x < v_s t \\ [n_r, 0]^T & \text{if } x > v_s t, \end{cases} \tag{18}$$

where the maximum velocity v_m is the solution of

$$(1 - n_r \exp(v_m))(v_m^2 - 2v_m - 2\log(n_r)) - 2v_m^2 = 0$$

and the shock velocity v_s is given by

$$v_s = \frac{v_m}{1 - n_r \exp(v_m)}.$$

The solution (18) is obtained by imposing the usual jump conditions

$$v_s(\mathbf{u}^+ - \mathbf{u}^-) = \mathbf{f}(\mathbf{u}^+) - \mathbf{f}(\mathbf{u}^-)$$

on the system (17). The shock velocity increases as n_r becomes smaller. In particular, we have the limit shock velocities $v_s = 1$ as $n_r \to 1$ and $v_s = -1 + \sqrt{1 - 2\log(n_r)}$ as $n_r \to 0$.

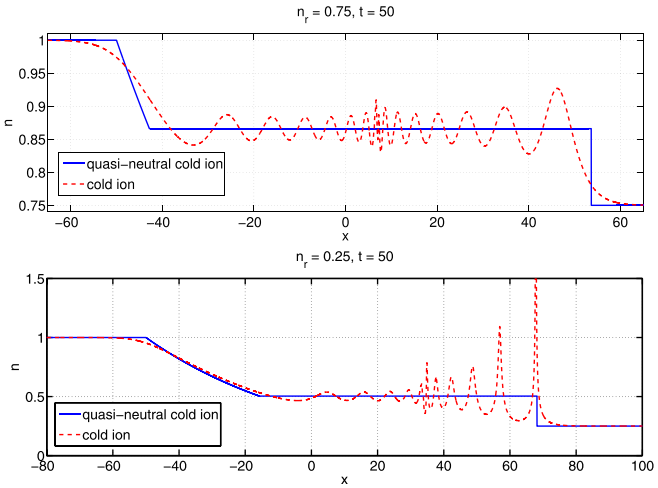

FIG. 1. Comparison between the self-similar solution (solid blue line) of the quasi-neutral approximation with the cold-ion solution (dashed red line) at $t = 50$ for $n_r = 0.75$ (top) and $n_r = 0.25$ (bottom). Top pair: $t = 20$; bottom pair: $t = 50$; top of each pair: $n_r = 0.75$; and bottom of each pair: $n_r = 0.25$.

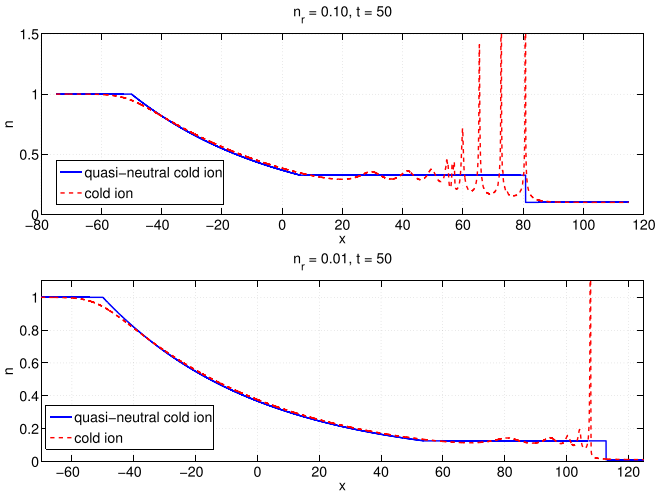

FIG. 2. Comparison of the cold-ion solution with the quasi-neutral solution at $t = 50$ for $n_r = 0.1$ (top) and $n_r = 0.01$ (bottom).

We expect that the cold-ion solution matches the self-similar solution as $x \to \pm\infty$ (numerical evidence is provided in Figures 1 and 2). In particular, we expect that $\phi(-\infty) = 0$ and $\phi(\infty) = \ln(n_r)$ and that $\lambda^{\pm} \to \pm 1$ as we move away from the origin. This observation is useful in the numerical treatment of the cold-ion problem for which one needs to impose boundary conditions at the boundary of a finite computational domain.

C. Numerical results for the cold-ion model

1. Dependence on n_r

The numerical algorithms used to solve the cold-ion model are described in Appendix, Subsection 1. We present, in Figures 3 and 4, numerical results for the present problem in the cold-ion limit for different values of n_r. For values of n_r close to unity, we expect the solution of the problem to be close to the one of the linearized system to be presented in Sec. III A. This is confirmed

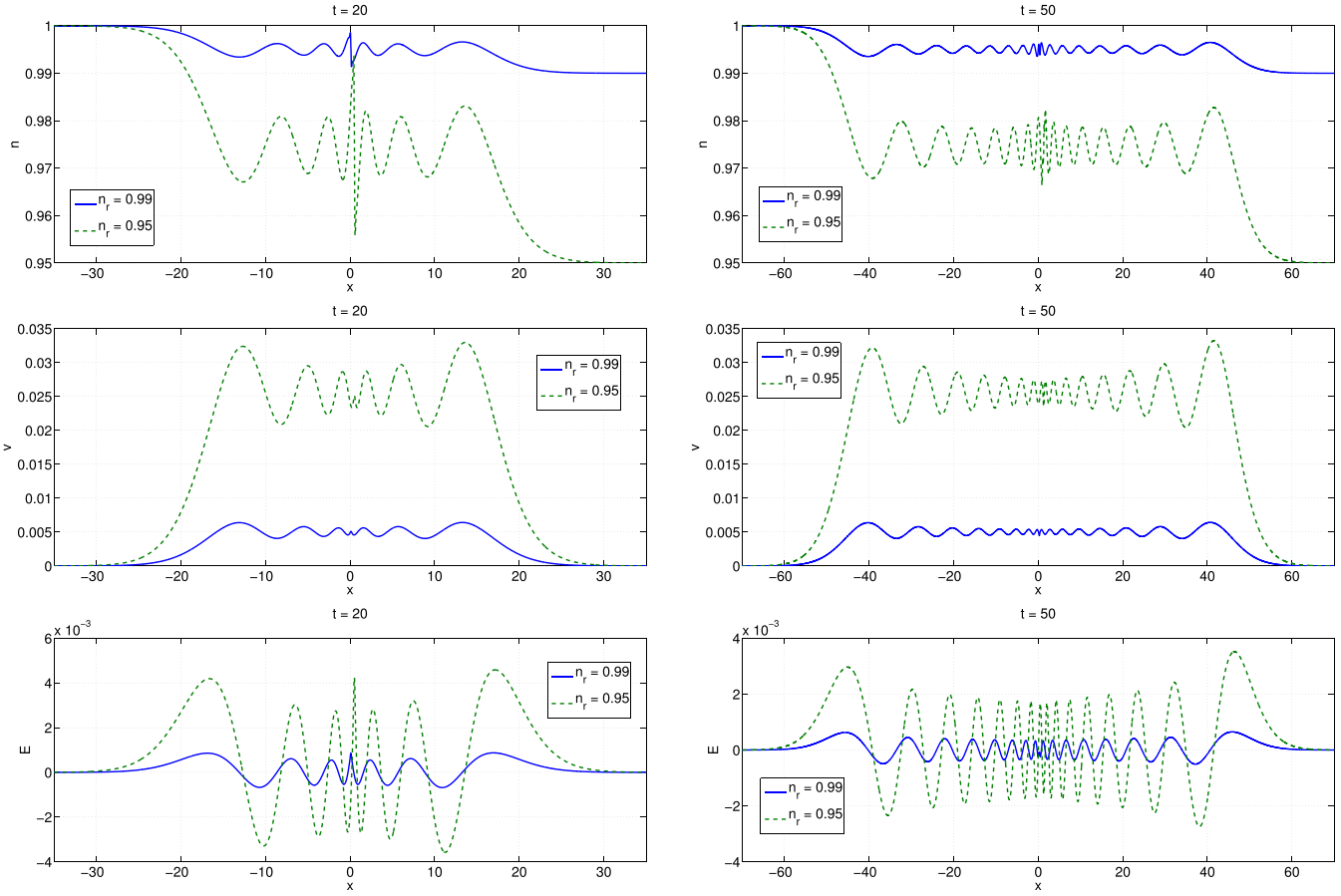

FIG. 3. Cold-ion solution for $n_r = 0.99$ (solid blue line) and $n_r = 0.95$ (dashed green line). From top to bottom: ion density n, velocity v, and electric field E. From left to right: $t = 20$ and $t = 50$.

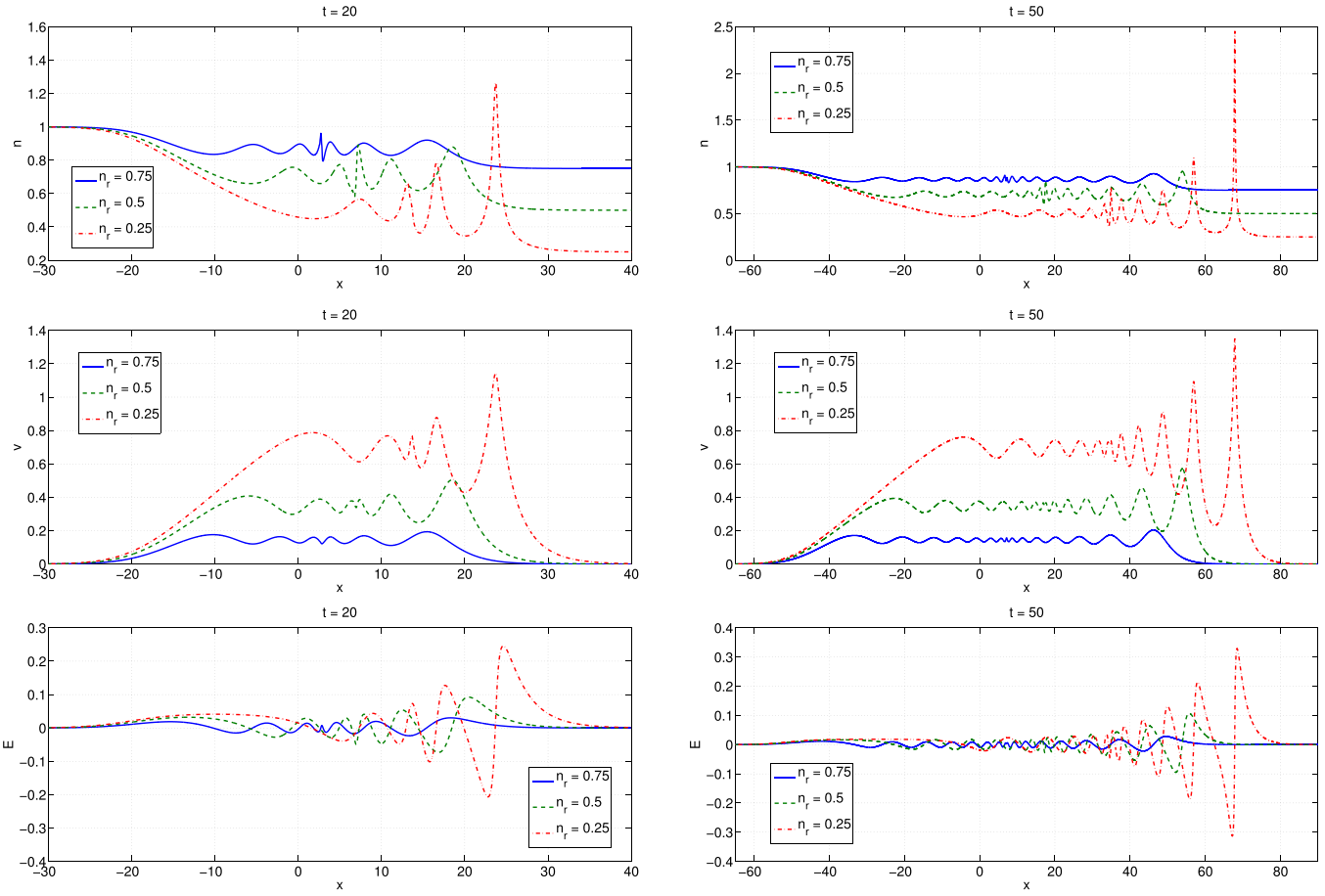

FIG. 4. Cold-ion solution for $n_r = 0.75$ (solid blue line), $n_r = 0.5$ (dashed green line), and $n_r = 0.25$ (dotted-dashed red line). From top to bottom: ion density n, velocity v, and electric field E. From left to right: $t = 20$ and $t = 50$.

by the comparison of the cold-ion solution with the linearized one shown in Figure 5. Moreover, the concentration of short wavelengths near the origin is in accordance with the fact that the group velocity associated with (16) tends to zero as $k \to \infty$.

As n_r becomes smaller, we observe that the cold-ion solution propagates faster and has fewer oscillations. This trend is observed in particular in Figure 4. Also, we observe that the trailing part of the wave has increasing amplitude as n_r decreases and as time increases. In Sec. II C 2, we investigate this phenomenon for small values of n_r.

It is worth comparing the cold-ion solution with the quasi-neutral model presented in Sec. II B. The comparison is shown in Figure 1; the self-similar solution appears to be an "average" of the cold-ion solution. The correlation between the shock position in the self-similar solution and the first peak in the cold-ion solution is also remarkable.

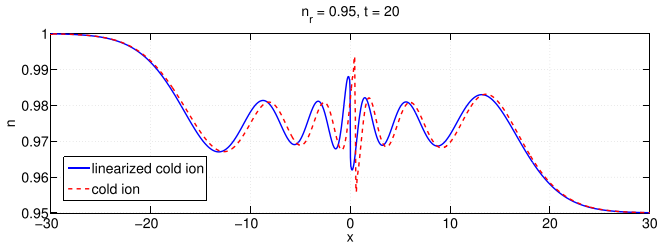

FIG. 5. Comparison between the cold-ion solution (dashed red line) and the linearized one (solid blue line) for $n_r = 0.95$. The contact discontinuity for the linearized solution is fixed at $x = 0$.

2. Small values of n_r

We next consider the case of small values of n_r. Figure 6 shows the cold-ion solution for $n_r = 0.1$ at $t = 10$, as the grid is refined. It is clear from Figure 6, top, that the ion concentration n is not converging as the grid is refined, whereas the other variables (v and E) seemingly converge. In Table II, we provide the L^1 and L^∞ norms of the difference of the solutions obtained with subsequent refinements. Figure 6 and Table II suggest that the leading peak has evolved into a "spike" that might correspond to a singularity in the solution and is not a computational artifact. In fact, as the spatial step size is decreased, the amplitude of the spike increases and its "width" decreases but its position does not significantly change. (These observations also hold for later plots which we refer to as having spikes.) In the review paper Ref. 13, the cold-ion equation is listed within a class of equations that can feature such singular solutions.

3. Expansion into a vacuum ($n_r = 0$)

When solving the cold-ion model for the case of expansion into vacuum, it is better to use a Lagrangian approach. The modified numerical scheme used when $n_r = 0$ is presented in Appendix, Subsection 2.

Figure 7 shows the numerical solution obtained with such scheme at $t = 10$. It is remarkable that the solution for

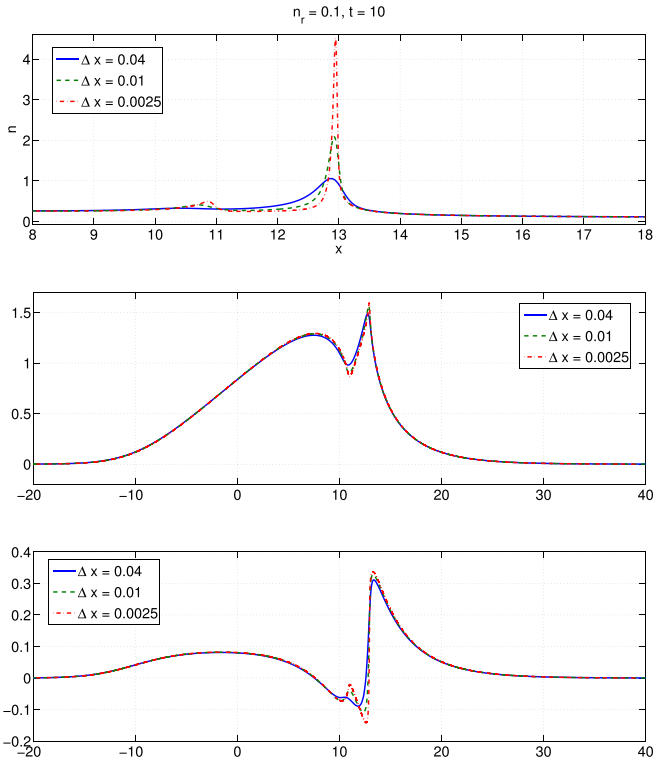

FIG. 6. Solution of the cold-ion model for $n_r = 0.1$ and $t = 10$ vs. the spatial discretization step Δx; top to bottom: n, v, and E.

the expansion into a vacuum does not exhibit any spikes, which is surprising given the results for small values of n_r given in Sec. II C 2. Such solution for the $n_r = 0$ case is in agreement with the results in Ref. 5. In particular, Figure 8 shows the nondimensionalized charge-separation (the difference between the ion and electron charges) at time $t = 50$, and reproduces the result in Figure 1 of Ref. 5.

These results suggest several limits in which our model may be susceptible to asymptotic analyses; we now present some of these.

III. LINEAR AND NONLINEAR ASYMPTOTIC ANALYSES OF THE COLD-ION MODEL

A. The linearized cold-ion model

When n_r is close to unity, we can then approximate the solution to the cold-ion models (10) and (14) by linearizing about $n = 1$, $\phi = 0$, and $v = 0$. If we define

$$n = 1 + \theta\tilde{n}, \quad v = \theta\tilde{v}, \quad \phi = \theta\tilde{\phi},$$

where $\theta = (1 - n_r)$, then, to leading order in θ, we obtain the linearized model equation

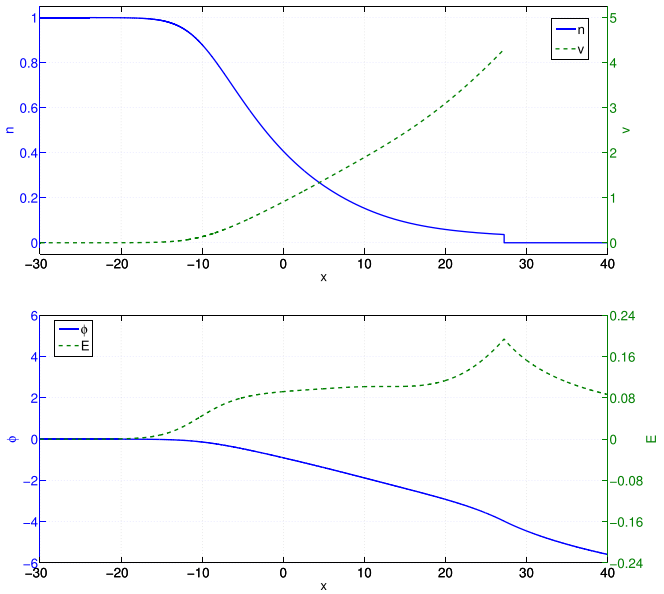

FIG. 7. Cold ion solution at $t = 10$ for $n_r = 0$; top: n (solid line) and v (dashed line); bottom: ϕ (solid line) and E (dashed line).

$$\frac{\partial^4 \tilde{n}}{\partial x^2\,\partial t^2} + \frac{\partial^2 \tilde{n}}{\partial x^2} - \frac{\partial^2 \tilde{n}}{\partial t^2} = 0. \tag{19}$$

The dispersion relation (16) follows directly from (19). The corresponding initial and far-field conditions are

$$\tilde{n}(x,0) = -\mathrm{H}(x), \quad \left.\frac{\partial \tilde{n}(x,t)}{\partial t}\right|_{t=0} = 0,$$

where H is the Heaviside function, and

$$\tilde{n}(x,t) \to \begin{cases} 0 & \text{as} \quad x \to -\infty, \\ -1 & \text{as} \quad x \to \infty. \end{cases}$$

By taking a Fourier transform in x, for example, the solution is found to be

$$\tilde{n}(x,t) = -\frac{1}{2} - \frac{1}{2\pi}\int_0^\infty \left\{ \sin\left(kx + \frac{kt}{\sqrt{1+k^2}}\right) + \sin\left(kx - \frac{kt}{\sqrt{1+k^2}}\right) \right\} \frac{\mathrm{d}k}{k}. \tag{20}$$

This approximate solution is compared with numerical solutions of the full cold-ion model in Figure 5 with $n_r = 0.95$ and $t = 20$. As expected, the two solutions are almost superimposed. However, while the contact discontinuity in the linearized solution (20) is fixed at $x = 0$, the contact

TABLE II. For $n_r = 0.1$ and $t = 10$, the L^∞ and L^1 norm of the difference of solutions obtained with subsequent grid refinements; the Courant number = 0.9.

		$\|n_{\Delta x_1} - n_{\Delta x_2}\|$		$\|v_{\Delta x_1} - v_{\Delta x_2}\|$		$\|\phi_{\Delta x_1} - \phi_{\Delta x_2}\|$		$\|E_{\Delta x_1} - E_{\Delta x_2}\|$	
Δx_1	Δx_2	$\|\cdot\|_\infty$	$\|\cdot\|_1$	$\|\cdot\|_\infty$	$\|\cdot\|_1$	$\|\cdot\|_\infty$	$\|\cdot\|_1$	$\|\cdot\|_\infty$	$\|\cdot\|_1$
4×10^{-2}	2×10^{-2}	0.399	0.228	0.0587	0.175	0.0187	0.123	0.0585	0.0824
2×10^{-2}	1×10^{-2}	0.660	0.218	0.0456	0.111	0.0166	0.0920	0.0650	0.0675
1×10^{-2}	5×10^{-3}	1.027	0.199	0.0341	0.0786	0.0138	0.0708	0.0664	0.0521
5×10^{-3}	2.5×10^{-3}	1.495	0.178	0.0316	0.0637	0.0108	0.0589	0.0639	0.0405

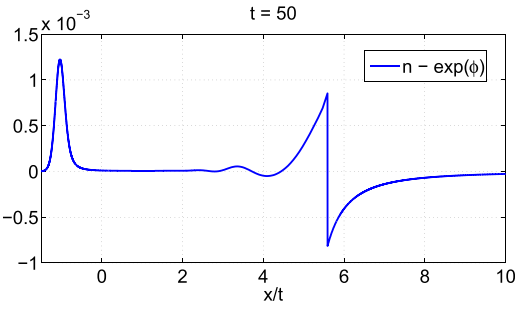

FIG. 8. The charge separation $(n - \exp(\phi))$ at $t = 50$ as a function of $\frac{x}{t}$.

discontinuity in the nonlinear cold-ion solution propagates slowly in the positive x-direction.

The linearized solution plotted in Figure 5 displays a growing train of ion-acoustic waves propagating away from the initial discontinuity, with the wave-front propagating at approximately unit speed. This qualitative behavior may be further elucidated by analyzing the integral in (20) in the asymptotic limit $t \to \infty$. A standard stationary-phase analysis then gives the dominant behavior of (20) in the form

$$\tilde{n}(x,t) \sim -\frac{1}{2} - \frac{t^{1/3}\sin\left(\pi/4 - (t^{2/3} - x^{2/3})^{3/2}\right)}{\sqrt{6\pi}\,x^{1/3}(t^{2/3} - x^{2/3})^{3/4}}$$
$$\text{for } -t < x < 0 \text{ and } 0 < x < t. \tag{21}$$

Figure 9 shows that this approximation successfully captures the train of ion-acoustic waves and correctly predicts the existence of a wave-front approximately at $x = t$. However, the approximation becomes invalid in layers near $x = 0$ and $x = \pm t$.

Considering first the limit $x \to 0$, we find that a distinguished limit occurs when $x = O(t^{-1/2})$ as $t \to \infty$, in which case

$$\tilde{n}(x,t) \sim -\frac{1}{2} - \frac{\mathrm{sgn}(x)}{2\pi}\mathrm{Im}\left\{e^{it}\int_{-\infty}^{\infty} e^{i\eta(s-1/s^2)}\frac{ds}{s}\right\},$$
$$\text{where } \eta = \left(\frac{x^2 t}{2}\right)^{1/3} \tag{22}$$

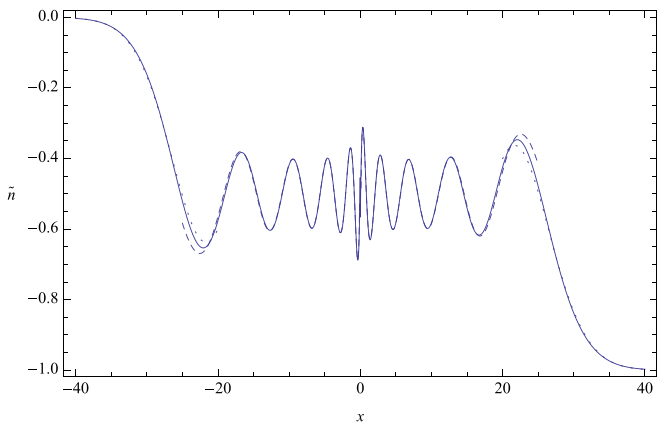

FIG. 9. The ion density perturbation $\tilde{n}$ plotted versus x at $t = 30$; solid: exact solution (20); dashed: large-t approximation (21); dotted: wave-front approximation (23).

and $\eta = O(1)$ as $t \to \infty$. In particular, this implies that

$$\tilde{n}(0\pm, t) = -\frac{1}{2} \mp \frac{\cos t}{2},$$

confirming that the contact discontinuity at $x = 0$ persists for all time in the linearized model. One can also easily verify that (22) matches with (21) as $\eta \to \infty$.

On the other hand, as $x \to t$, the relevant scaling is found to be $x - t = O(t^{1/3})$, in which case the leading-order approximation to (20) is given by

$$\tilde{n} \sim -1 + g((x-t)t^{-1/3}), \quad \text{where}$$
$$g(\xi) = \frac{1}{4} - \frac{1}{2\pi}\int_0^{\infty} \sin\left(\frac{s^3}{2} + \xi s\right)\frac{ds}{s}, \tag{23}$$

and $\xi = O(1)$ as $t \to \infty$. The corresponding behavior as $x \to -t$ is easily inferred by symmetry. This is shown as a dotted curve in Figure 9, where we see that it too agrees well with the true solution (20) near the wave-front at $x = t$.

These results show that, in the limit as $n_r \to 1$, the amplitude of the waves remains bounded for all time, and there is no indication of any spikes forming in the solution. However, this leaves open the potential for nonlinear effects to accumulate over a long time-scale to produce spikes. To examine this possibility, we next perform a weakly nonlinear analysis.

B. Weakly nonlinear cold-ion model

The result (23) for the linearized behavior near $x = t$ motivates the large-time scaling

$$T = \theta^{3/2}t, \quad X = \theta^{1/2}(x - t),$$

and we define the corresponding local dependent variables as

$$n(x,t) = 1 + \theta N(X,T),$$
$$\phi(x,t) = \theta\Phi(X,T),$$
$$v(x,t) = \theta V(X,T).$$

This transforms the cold-ion models (10) and (14) into

$$\frac{\partial N}{\partial X} + \frac{\partial V}{\partial X} = \theta\left[\frac{\partial N}{\partial T} + \frac{\partial (NV)}{\partial X}\right],$$
$$\frac{\partial V}{\partial X} - \frac{\partial \Phi}{\partial X} = \theta\left[\frac{\partial V}{\partial T} + V\frac{\partial V}{\partial X}\right], \tag{24}$$
$$\Phi + N = \theta\left[\frac{\partial^2 \Phi}{\partial X^2} - \frac{\Phi^2}{2}\right] + O(\theta^2).$$

By using the leading-order downstream far-field conditions

$$N \to 1, \quad V \to 0, \quad \Phi \to -1 \quad \text{as} \quad X \to \infty,$$

we therefore obtain

$$N = V - 1 = \Phi,$$

to leading order in θ. We then combine the equations in (24) to eliminate the dominant left-hand sides and thus find that $V(X, T)$ satisfies

$$\frac{\partial V}{\partial T} + V\frac{\partial V}{\partial X} + \frac{1}{2}\frac{\partial^3 V}{\partial X^3} = 0, \tag{25}$$

which is equivalent to the KdV equation. Matching with (23) gives the initial condition

$$V(X,T) \to \frac{1}{2}\mathrm{H}(-X) \quad \text{as} \quad T \to 0 \tag{26}$$

and the far-field conditions are

$$V(X,T) \to \begin{cases} 0 & \text{as} \quad X \to \infty, \\ 1/2 & \text{as} \quad X \to -\infty. \end{cases}$$

The early time response is given by a similarity solution of the form

$$V(X,T) \sim g(XT^{-1/3}) \quad \text{as} \quad T \to 0,$$

where

$$g(\xi) = \frac{1}{2}\int_{(2/3)^{1/3}\xi}^{\infty} \mathrm{Ai}(s)\,\mathrm{d}s,$$

with Ai denoting an Airy function of the first kind. It can be verified that this $g(\xi)$ is identical to the function defined by (23), so that the small-time behavior of the solution to (25) successfully matches with (20).

It is known[18] that solutions of (25) are regular for all $T > 0$, even for the discontinuous initial data (26). Hence, even when nonlinear effects are included, there is no sign of a singularity forming in the solution when n_r is sufficiently close to 1.

C. Blow-up behavior

The analysis carried out above indicates that the ion density remains smooth and bounded for all time if n_r is close to unity. However, for smaller values of n_r, the numerical results presented in Sec. II C display spikes, where n is apparently unbounded. We can provide further evidence for this behavior by seeking local solutions of (10) and (14) in which n, v, and ϕ are smooth functions of x for $t < t_*$ but $\sup_x n \to \infty$ as $t \nearrow t_*$, where t_* is some critical spike formation time. Let the maximum of $n(x,\,t)$ occur at $x = s(t)$ for each $t < t_*$. Then, the local behavior near $x = s(t)$ as $t \nearrow t_*$ can be described by a similarity solution of (10) and (14) in which

$$n = (t_* - t)^{-1}F(\eta), \tag{27a}$$

$$v = \dot{s}(t) + (t_* - t)^{1/2}G(\eta), \tag{27b}$$

$$\phi = \phi_0(t) - E_0(t)(x - s(t)) + (t_* - t)^2 H(\eta), \tag{27c}$$

where

$$\eta = \frac{x - s(t)}{(t_* - t)^{3/2}}, \quad \phi_0(t) = \phi(s(t),t), \quad E_0(t) = E(s(t),t).$$

Substituting (27) into (10) and (14) and letting $t \nearrow t_*$, we find that

$$F(\eta) = \frac{A}{1 + 3BG(\eta)^2}, \tag{28a}$$

$$H(\eta) = -\frac{A}{4}G(\eta)^2\left(2 + 3BG(\eta)^2\right), \tag{28b}$$

where the function $G(\eta)$ satisfies the implicit equation

$$G(\eta) + BG(\eta)^3 = -\eta. \tag{28c}$$

The positive integration constants A and B remain arbitrary in this local analysis and can be determined only by matching with the (numerical) solution of the full initial-value problem. In any case, they can be normalized out of the local behavior by the scalings

$$\eta = \frac{\tilde{\eta}}{B^{1/2}}, \quad F = A\tilde{F}, \quad G = \frac{\tilde{G}}{B^{1/2}}, \quad H = \frac{A\tilde{H}}{B}, \tag{29}$$

so no generality is lost by henceforth setting $A = B = 1$.

In Figure 10, we plot the functions $F(\eta)$, $G(\eta)$, and $H(\eta)$ defined by (28). The local behavior of the ion density n is determined by the function $F(\eta)$, which is an even function with a maximum as expected at $\eta = 0$ and $F(\eta) \sim 1/3|\eta|^{2/3}$ as $\eta \to \pm\infty$. The local relative velocity is described by the odd function $G(\eta)$ with limiting behaviors $G(\eta) \sim -\eta$ as $\eta \to 0$ and $G(\eta) \sim -\eta^{1/3}$ as $\eta \to \pm\infty$. Finally, the function $H(\eta)$, describing the perturbation to the local electric potential, is even, with a maximum at $\eta = 0$ and $H(\eta) \sim -3|\eta|^{4/3}/4$ as $\eta \to \pm\infty$.

These limits imply that

$$n \sim \frac{1}{3(x - s)^{2/3}} \quad \text{as } t \nearrow t_*. \tag{30}$$

This implies that, although the ion density tends to infinity, its integral is finite and n does *not* approach a delta distribution. This in turn implies that the electric field E and potential ϕ are continuous across the spike.

We now perform a preliminary numerical verification of this local analysis near the singularity, focusing on the illustrative case $n_r = 0.1$. In Figure 11, a comparison between the numerical cold-ion solution and the local solution (27) is shown for different values of t. In these plots, A, B, and t_* are independent of t and have been estimated by fitting the computed solution n at different times with the predicted local

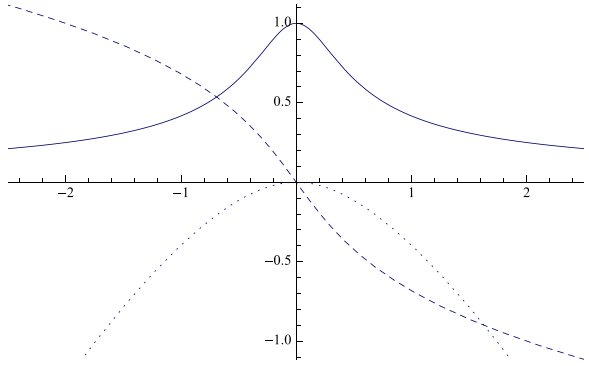

FIG. 10. The functions $F(\eta)$ (solid), $G(\eta)$ (dashed), and $H(\eta)$ (dotted) defined by (28).

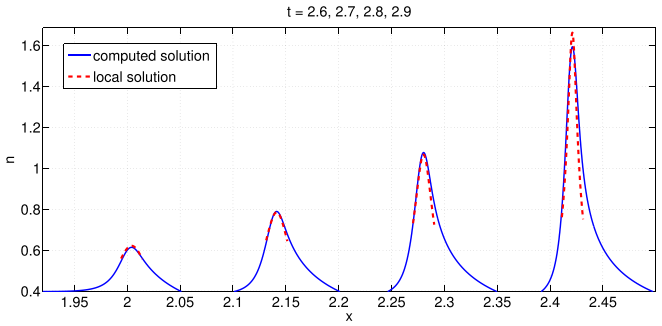

FIG. 11. Comparison between the computed cold-ion density n and the local solution (27), with $t_* = 3.08$, $A = 0.298$, and $B = 44.7$.

behavior (27a) for x in $(s - 0.01, s + 0.01)$, s being the argmax of n. The numerical solution and the local asymptotic solution for the ion density are seemingly in agreement, and this mutual corroboration supports the assertion that the cold-ion model does admit solutions, which form spikes in finite time.

These results prompt us to question the validity of the cold-ion model once the solution has formed a spike. To gain further insight into this question, in Sec. IV, we consider simulations of the Vlasov-Poisson systems (9)–(13), in particular when ε is nonzero but small. Our aim is to determine whether or not the Vlasov-Poisson solutions converge to the corresponding cold-ion solutions as the ion temperature tends to zero.

IV. VLASOV-POISSON SYSTEM FOR NONZERO ION TEMPERATURE

The previous sections pose several unanswered questions concerning the cold-ion model and we now attempt to resolve them by regularizing the model by reinstating the ion temperature. Thus, we return to the dimensionless Vlasov equation, which is solved using the numerical scheme described in Appendix, Subsection 3.

A. Numerical results

We consider the initial conditions (12) and (13) for different values of n_r and ε. Figure 12 shows a surface plot of f as a function of x and v at $t = 30$ for $n_r = 0.75$ and 0.1 and $\varepsilon = 0.1$ and 0.025. When the temperature ratio ε is small, we are close to the cold-ion limit, and at $t = 0$, the ions are concentrated in a small v-neighborhood of the x axis, whereas for larger ε, the initial ion distribution is less localized. This is reflected in the solution at later times as can be seen comparing the left- to the right-hand plots in Figure 12.

The "advection" field of the Vlasov equation is [v, $E(x)$]. At $t = 0$, the electric field $E(x)$ is positive in the neighborhood of the discontinuity located at $x = 0$. Hence, ions first drift in the direction of the v-axis with velocity $E(x)$ and, for $t > 0$, in the direction of the x-axis with velocity v. Also, (i) as n_r decreases, E increases, and n becomes less

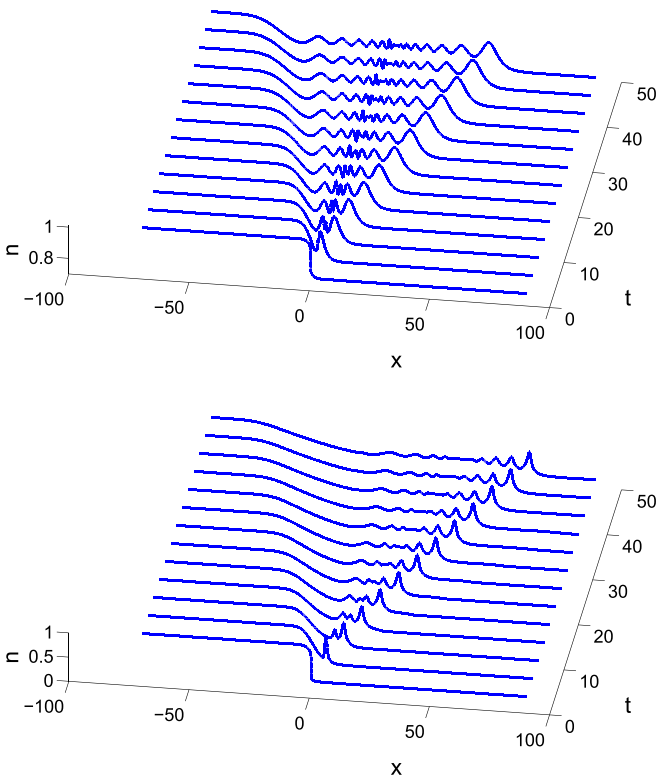

FIG. 13. Ion density n as a function of x at several time instants for $\varepsilon = 0.025$ for an initial ion density $n_r = 0.75$ (top) and $n_r = 0.25$ (bottom).

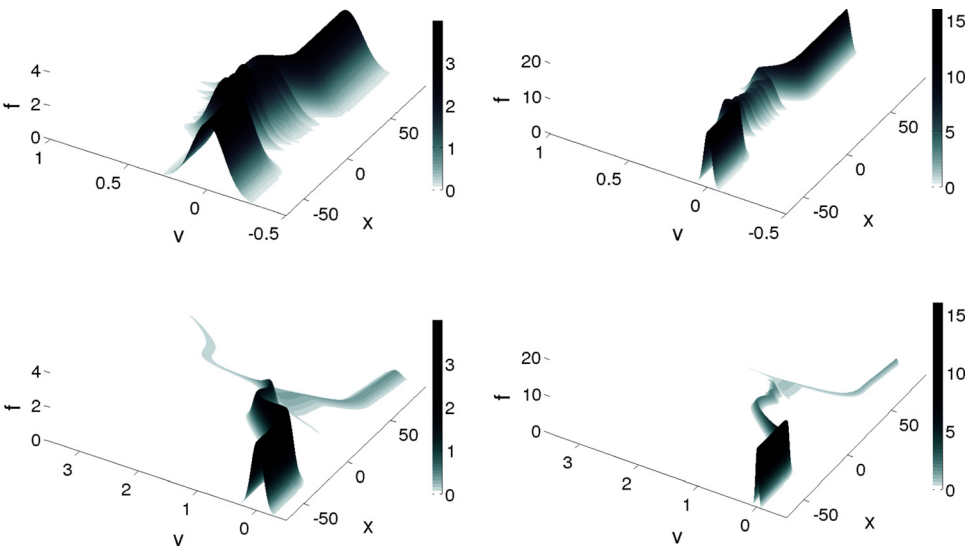

FIG. 12. Ion distribution function f at $t = 30$ for $n_r = 0.75$ (top row) and $n_r = 0.1$ (bottom row) and for $\varepsilon = 0.1$ (left column) and $\varepsilon = 0.025$ (right column).

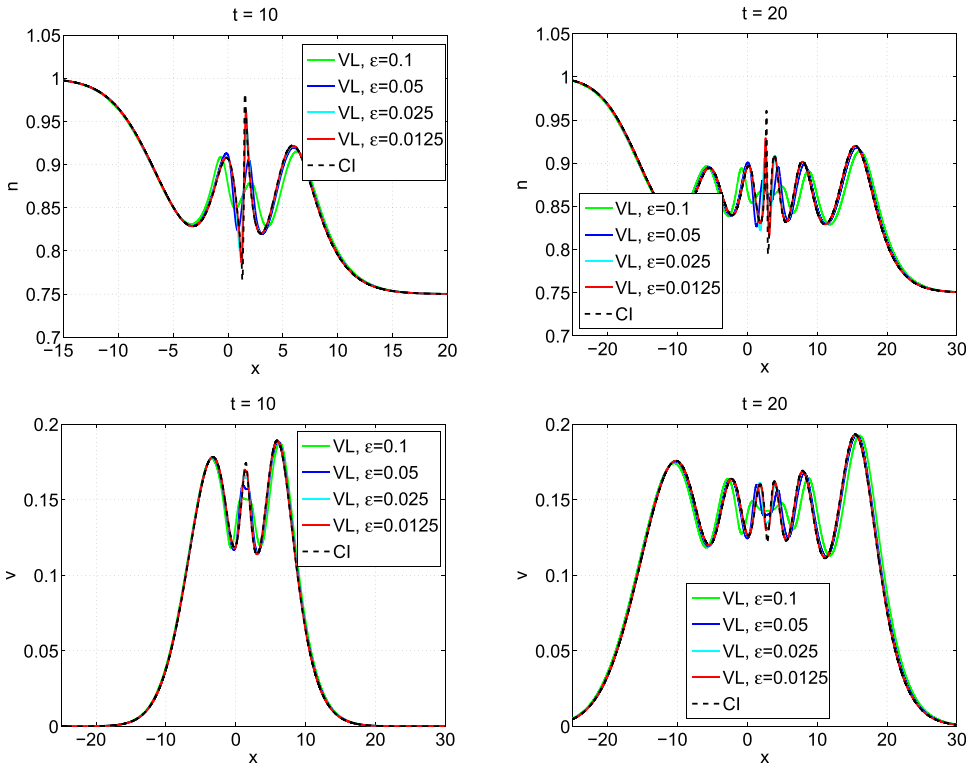

FIG. 14. For $n_r = 0.75$, comparison between the Vlasov-Poisson solution for different values of ε and the cold-ion solution; top row: n; bottom row: v; left column: $t = 10$; right column: $t = 20$.

oscillatory (see Figure 13); (ii) as n_r decreases, n is concentrated at faster velocities; (iii) the plot of $n(x, t)$ in Figure 13 resembles the cold-ion solution. Most strikingly, for $n_r = 0.1$, the support of the ion distribution f in the (x, v) plane displays a bifurcation.

B. Comparison with the cold-ion limit

We now investigate the solution of the Vlasov-Poisson system as the ratio ε between the ion and electron temperatures goes to zero. Figure 14 shows n and v for $n_r = 0.75$, obtained from the integration (with respect to v) of the solution of the Vlasov-Poisson system, superimposed on the values from the cold-ion model. Figure 15 shows the L^1 norm of the difference between the Vlasov-Poisson and cold-ion solutions as a function of ε. The results indicate a linear convergence rate for n and a superlinear rate ($\approx$1.5) for v.

Figures 16 and 17 show the same comparisons for $n_r = 0.25$, revealing that the convergence of the integrated Vlasov-Poisson solution to the cold-ion solution is less evident, especially for v. The L^1 norm convergence rates at earlier time instants are similar to those obtained for $n_r = 0.75$. However, for later times, the convergence rate is close to 0.5 for n and between 0.5 and 1 for v.

Most interesting is Figure 18, where n_r is further reduced to 0.1 and the Vlasov-Poisson solution does not seem to converge to the cold-ion solution. In particular, the Vlasov-Poisson solution propagates more slowly than the cold-ion solution and the velocity v is quite different in the two cases.

Figure 19 shows, for $\varepsilon = 0.025$, the behavior of the Vlasov-Poisson solution as n_r approaches zero and for $n_r = 0$; also shown is the cold-ion solution for $n_r = 0$, which is almost superimposed on the Vlasov-Poisson solution in the vacuum case. We observe that, as n_r tends to zero, the oscillations in n vanish and the velocity increases.

We summarize the results of this section about the convergence of the numerical solutions of the Vlasov-Poisson system as $\varepsilon \to 0$ as follows.

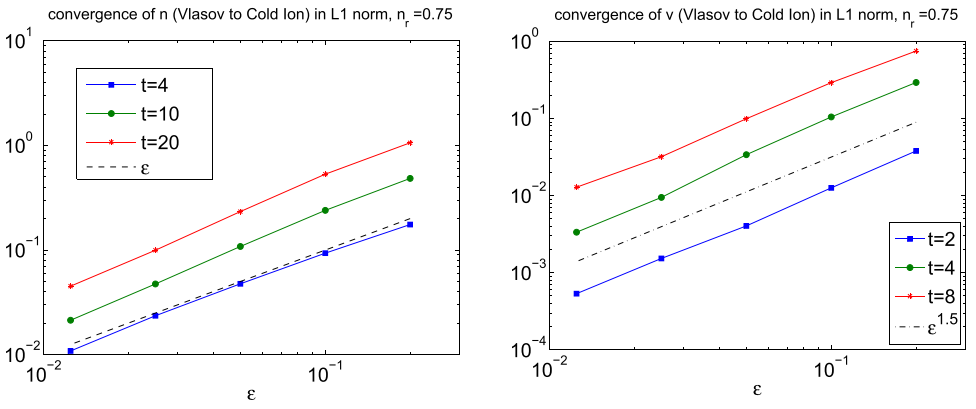

FIG. 15. L^1 norm of the difference between the Vlasov-Poisson and cold-ion solutions as a function of ε at different time instants for $n_r = 0.75$; left: n and right: v.

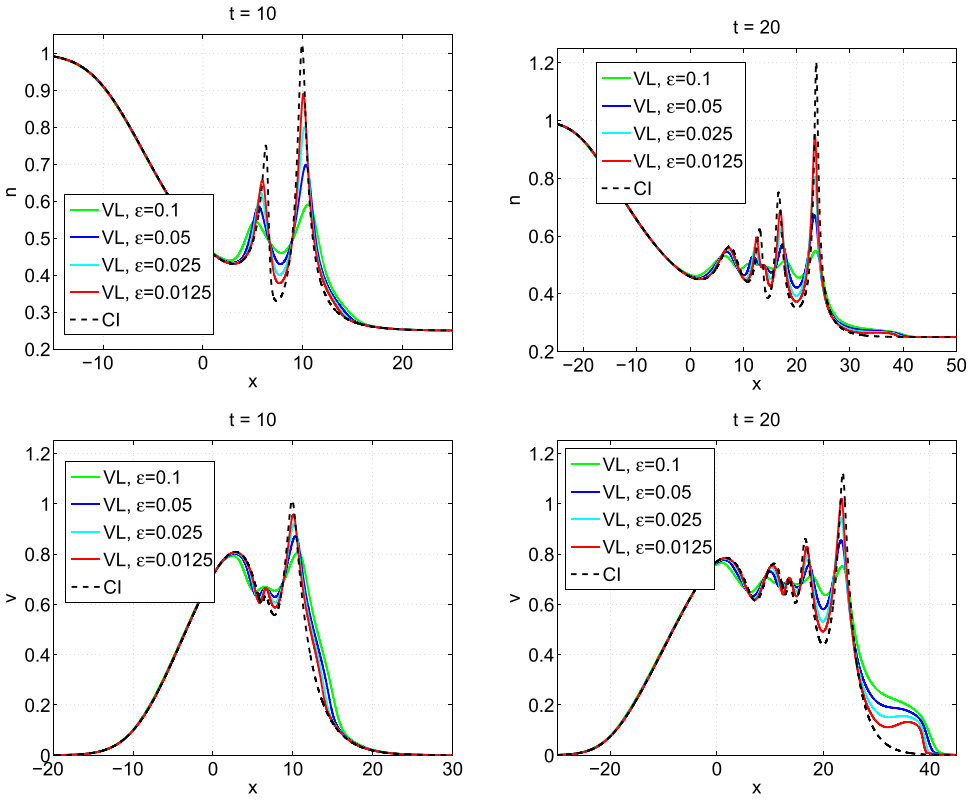

FIG. 16. For $n_r = 0.25$, comparison between the Vlasov-Poisson solution for different values of ε and the cold-ion solution; top row: n; bottom row: v; left column: $t = 10$; right column: $t = 20$.

- For n_r close to unity, the v-integrated Vlasov-Poisson solution converges to the cold-ion solution.
- For small $n_r > 0$, the v-integrated Vlasov-Poisson solution does not converge to cold-ion solution.
- In the vacuum case ($n_r = 0$), the v-integrated Vlasov-Poisson solution converges to the solution of cold-ion model.

It is no easy matter to determine numerically the value of n_r at which the transition from convergence to non-convergence to the cold-ion solution occurs nor of the nature of that transition. Also, at this time, we do not have a mathematical theory that supports these results. However, it is worthwhile to carefully look at the qualitative behavior of the ion distribution f for different values of n_r. Figure 20 shows the logarithm of f in regions where $f \geq 0.001$ at different time instants and for different initial ion densities. The temperature ratio ε is 0.025. When $n_r = 0.75$ (and greater), the solution consists of a single "stripe," mostly in the x direction. As $\varepsilon \to 0$, we expect the "stripe" to become thinner and reduce to a curve that is the support of $\delta(\mathrm{v} - v(x,t))$, i.e., the curve is expected to be the graph of the cold-ion velocity v. However, for smaller values of n_r, the ion distribution ceases to be unimodal; see Figure 20 for n_r ranging between 0.001 and 0.25. In this situation, the cold-ion solution is unlikely be the limit solution of Vlasov-Poisson solutions as $\varepsilon \to 0$ because the cold-ion solution assumes a unimodal ion distribution, namely $f(x,\mathrm{v},t) = n(x,t)\,\delta(\mathrm{v} - v(x,t))$. However, we observe that as n_r decreases, fewer ions are present in the low-velocity branch, whereas more ions are in the high-velocity branch. Finally, when $n_r = 0$, all the ions are seemingly in the high-velocity branch and the distribution is unimodal again. Figure 21 shows that

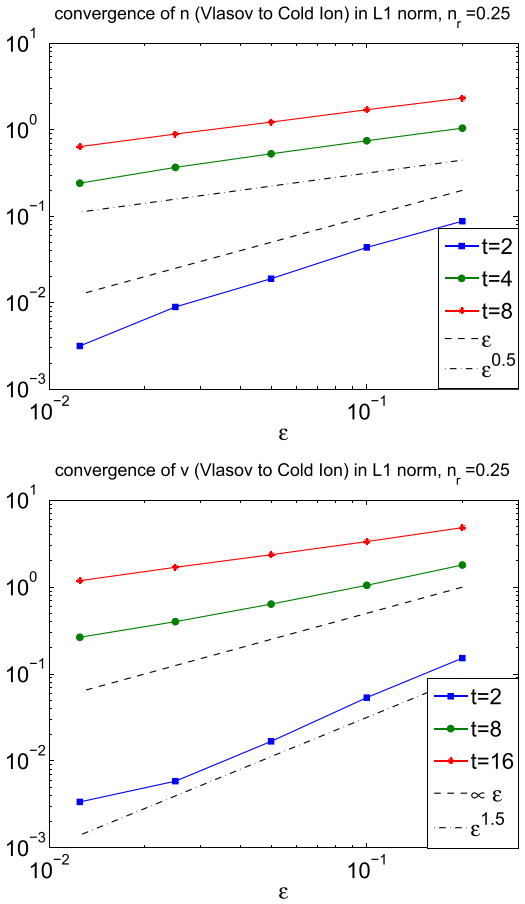

FIG. 17. For $n_r = 0.25$, the L^1 norm of the difference between the Vlasov-Poisson and cold-ion solutions as a function of ε at different time instants; top: n and bottom: v.

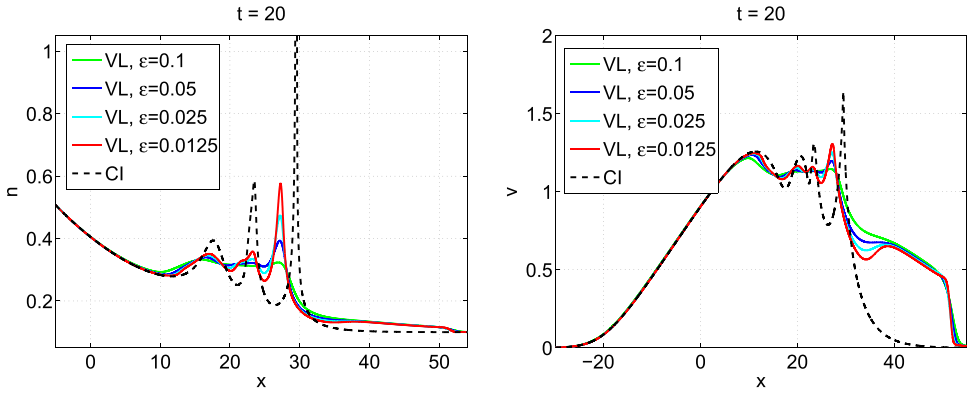

FIG. 18. For $n_r = 0.1$ and $t = 20$, comparison between the Vlasov-Poisson solution for different values of ε and the cold-ion solution; left: n and right: v.

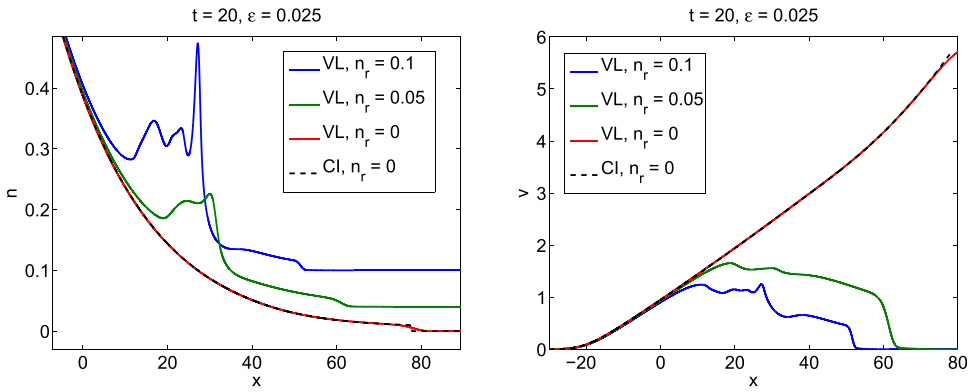

FIG. 19. For $\varepsilon = 0.025$ and $t = 20$, the Vlasov-Poisson solution for different values of n_r and the cold-ion model solution for $n_r = 0$ obtained using the Lagrangian approach; left: ion density n and right: ion velocity v.

similar behaviors are observed when the ion temperature is higher ($\varepsilon = 0.1$). That figure, when compared to Figure 20, also clearly shows the thinning and the increase in height of the spike for the smaller value of ε.

The ion distribution behaviors observed in Figures 20 and 21 help explain the convergence and lack of convergence results observed in this section. The formation of a spike in the cold-ion model corresponds to a wave-breaking phenomenon, as found previously by Ref. 6, whereby the distribution function f becomes multimodal and is no longer described by the classical cold-ion theory. We thus hypothesize that our cold-ion model is not correct (in the sense that its solution is not the Vlasov-Poisson solution in the cold-ion limit) for n_r in some interval $L \subset (0, 1)$. Unfortunately, it is very difficult to determine, even approximately, the set L numerically. We cannot even exclude the possibility $L = (0, 1)$ as it may indeed be possible that the distribution is multimodal also for n_r close to 1, but that the quantitative contribution of the secondary modes is so small as to not be detectable by our simulations.

V. CONCLUDING REMARKS

The picture that has emerged from this investigation is that, in the cold-ion limit, the expansion of a collisionless plasma into a plasma of lower density can be treated analytically and numerically by using the model (10) and (14) just as long as the density ratio is either zero or close to unity. In the latter case, a weakly nonlinear analysis suggests that soliton-like behavior occurs for large times, and in the former, no wave steepening occurs. For intermediate values of the density ratio, a finite-time singularity forms in the cold-ion model, in which the ion density develops a spike that has zero charge, i.e., is weak compared to a delta function. Thus, the electric field is continuous from one side of the spike to the other.

As soon as a spike forms, the cold-ion model ceases to be the limit of the Vlasov-Poisson system as the ion temperature T_i tends to zero. Numerical solutions of the Vlasov-Poisson system for $T_i > 0$ indicate that spike formation is intimately associated with the ion-distribution function becoming multi-modal. This implies the impossibility of using the cold-ion models (10) and (14) with a single-valued velocity v after a spike has formed.

Our picture is far from complete and leaves open many interesting challenges:

- A more precise delineation of the range for n_r or, more generally, the set of initial conditions for which spike formation occurs.
- When spike formation does occur, the dependence of the formation time on n_r, which appears to be an increasing function that is non-zero as $n_r \to 0$.
- The possibility of creating a multi-modal cold-ion model for the small-T_i limit of the Vlasov-Poisson system after spikes have formed.
- An analysis of the case with different species of positive ions, which would be relevant to experiments with laser-produced plasmas.
- The relaxation of assumption (1) about the electron density so as to describe plasmas for which the ion velocity is comparable to the electron thermal velocity.

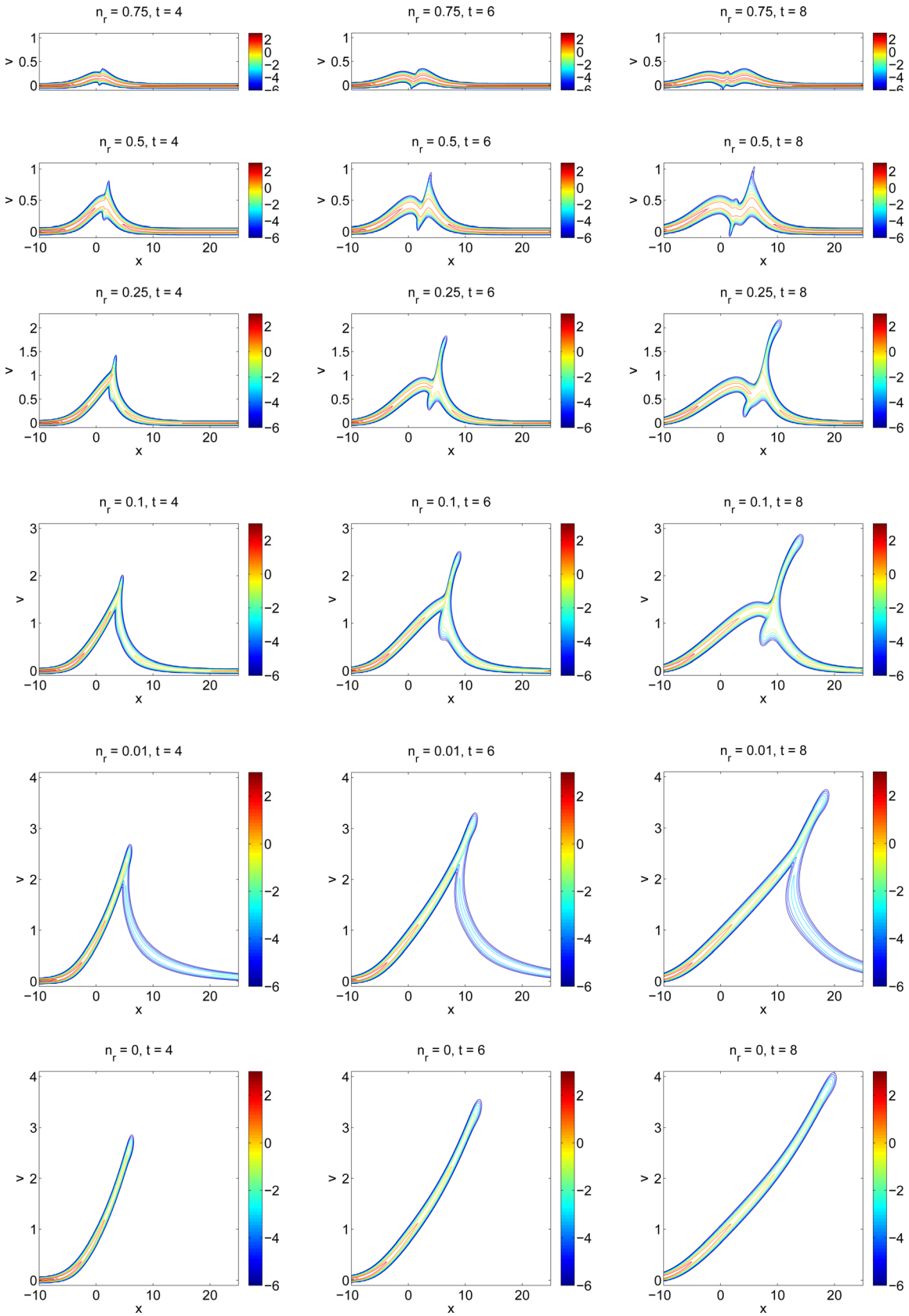

FIG. 20. For $\varepsilon = 0.025$, the logarithm of Vlasov-Poisson solution $[\log(f)]$ for different values of n_r and at different time instants. From left to right: $t = 4$, 6, and 8. From top to bottom, $n_r = 0.75$, 0.5, 0.25, 0.1, 0.01, and 0.

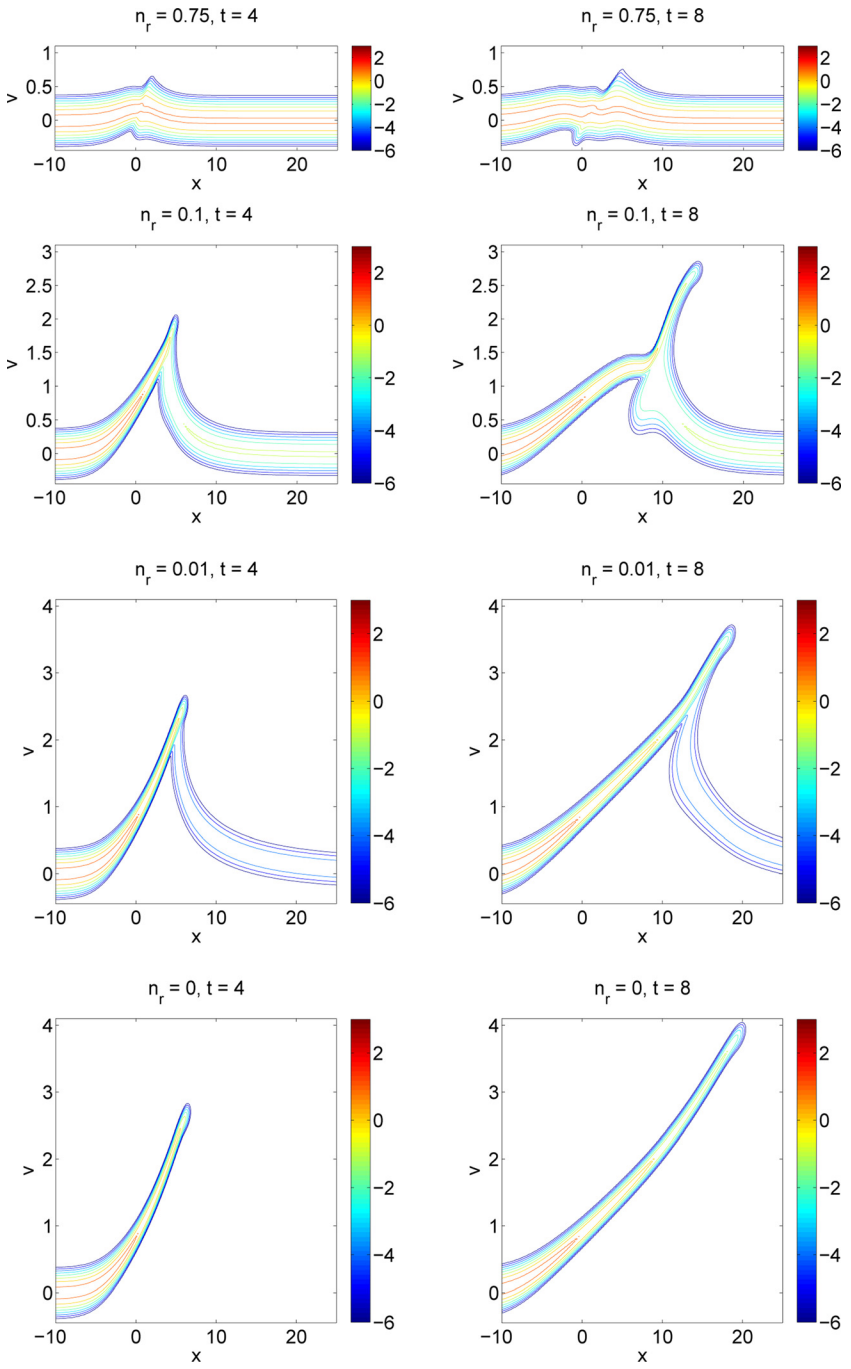

FIG. 21. For $\varepsilon = 0.1$, the logarithm of Vlasov-Poisson solution $[\log(f)]$ for different values of n_r and at different time instants. From left to right: $t = 4$ and 8. From top to bottom, $n_r = 0.75, 0.1, 0.01,$ and 0. These plots should be compared to the first and fourth columns of Figure 20.

ACKNOWLEDGMENTS

J. Ockendon acknowledges receipt of a Leverhulme Emeritus Fellowship during the course of this research.

APPENDIX: NUMERICAL METHODS

1. Numerical algorithms for cold ion model

The finite computational domain is given by the interval $I = [x_l, x_r]$. Two related grids enter into the numerical scheme we use to approximate solutions of (10) and (17). First, consider the partition of I into the J sub-intervals $I_j = [x_j, x_{j+1}]$, $j = 0, 1, \ldots, J-1$. The grid nodes, i.e., the end points of the sub-intervals, are given by $x_j = x_l + j\Delta x$, $j = 0,1,\ldots,J$, where $\Delta x = (x_r - x_l)/J$, so that $x_0 = x_l$ and $x_J = x_r$. We also use the staggered grid defined by the partition of $\tilde{I} = [x_l + \frac{\Delta x}{2}, x_r - \frac{\Delta x}{2}]$ into the $J-1$ sub-intervals $\tilde{I}_j = [x_{j-\frac{1}{2}}, x_{j+\frac{1}{2}}]$, $j = 1,\ldots,J-1$, where, for $j = 0,\ldots,J-1$, we have that $x_{j+\frac{1}{2}} = \frac{x_j + x_{j+1}}{2} = x_l + (j+\frac{1}{2})\Delta x$.

We need discretizations of the Poisson equation (10) with respect to both grids. First, consider the primal grid $\{x_j\}_{j=0}^{J}$. Discretization is effected via a finite element method, using continuous piecewise-linear functions with respect to that grid; see, e.g., Refs. 14 and 15 for additional details about the finite element methods used. We denote by X^h the space of functions that are continuous on I and linear on each sub-interval I_j. Given n and letting

$$\mathcal{F}(\phi_h,\psi_h) := \int_I \frac{\partial\phi_h}{\partial x}\frac{\partial\psi_h}{\partial x}\,\mathrm{d}x + \int_I \exp(\phi_h)\,\psi_h\,\mathrm{d}x - \int_I n\,\psi_h\,\mathrm{d}x \quad \forall\,\phi_h,\psi_h \in X^h,$$

the approximation $\phi_h \in X^h$ of the solution of the Poisson problem is required to satisfy

$$\mathcal{F}(\phi_h,\psi_h) = 0 \quad \forall\,\psi_h \in X^h.$$

We use Newton's method to address the nonlinearity of the problem. The Jacobian $\mathcal{J}$ of $\mathcal{F}$ along the direction $\mu_{\phi,h}$ is given by

$$\mathcal{J}(\mu_{\phi,h},\phi_h,\psi_h) = \int_I \frac{\partial\mu_{\phi,h}}{\partial x}\frac{\partial\psi_h}{\partial x}\,\mathrm{d}x + \int_I \exp(\phi_h)\,\mu_{\phi,h}\,\psi_h\,\mathrm{d}x.$$

Given a starting guess $\phi_h^0 \in X^h(I)$, Newton's method consists of successively solving, for $\ell = 0, 1, \ldots$, the linear problem

$$\mathcal{J}(\mu_{\phi,h}^{\ell+1},\phi_h^\ell,\psi_h) = -\mathcal{F}(\phi_h^\ell,\psi_h) \quad \forall\,\psi_h \in X^h$$

for $\mu_{\phi,h}^{\ell+1} \in X^h$ and then setting

$$\phi_h^{\ell+1} = \phi_h^\ell + \mu_{\phi,h}^{\ell+1}.$$

The iteration is terminated when $|\mathcal{F}(\phi_h^{\ell+1},\cdot)|$ is sufficiently small, after which we set $\phi_h(n) = \phi_h^{\ell+1}$.

Discretization of (10) on the staggered grid $\{x_{j+\frac{1}{2}}\}_{j=0}^{J-1}$ proceeds in the same way, except that now it is based on the space $\tilde{X}^h$ of functions that are continuous on $\tilde{I}$ and linear on each subinterval $\tilde{I}_j$.

For the discretization of the system (17), we use a two-step variant[16] of the Lax-Friedrichs (LxF) finite difference method which, as implemented in Ref. 17, does not require the use of the Jacobian of $\mathbf{f}$. The scheme is a monotone dissipative method and damps the mid-range frequencies to a lesser extent compared to the original Lax-Friedrichs method. The algorithm, described as follows, is composed of a half step of the Lax-Friedrichs scheme followed by a half step of the same scheme on the staggered grid. Let Δt denote the time step and, for $k = 0, 1, \ldots$, let $t_k = k\Delta t$. The time step Δt used in the simulations is adaptively selected so that $\nu = 0.9$, where the global Courant number ν is given by $\nu = \max(\|\lambda^-\|_\infty, \|\lambda^+\|_\infty)\frac{\Delta t}{\Delta x}$. For $k = 0, 1, \ldots$ and $j = 0, 1, \ldots, J$, let $\mathbf{u}_j^k = [n_j^k, v_j^k]^T$ denote the sought-for approximation of $\mathbf{u}(x_j, t_k)$. Then,

for $k = 0, 1, \ldots$, given $\mathbf{u}_j^k$ for $j = 0, 1, \ldots, J$,

(1) set $n_h^k(x) \in X^h(I)$ to be the piecewise linear interpolating function such that $n_h^k(x_j) = n_j^k$ for $j = 0, 1, \ldots, J$.
(2) solve the discretized Poisson equation on $[x_l, x_r]$ to obtain $\phi_h(n_h^k)$.
(3) for $j = 0, \ldots, J$, set $\phi_j^k = \phi_h(n_h^k)|_{x=x_j}$.
(4) for $j = 0, \ldots, J$, set $\mathbf{f}_j^k = \mathbf{f}(\mathbf{u}_j^k) = \begin{bmatrix} n_j^k\, v_j^k \\ \frac{1}{2}(v_j^k)^2 + \phi_j^k \end{bmatrix}$.
(5) for $j = 0, \ldots, J-1$, compute

$$\mathbf{u}_{j+\frac{1}{2}}^{k+\frac{1}{2}} = \frac{1}{2}(\mathbf{u}_j^k + \mathbf{u}_{j+1}^k) + \frac{1}{2}\frac{\Delta t}{h}(\mathbf{f}_{j+1}^k - \mathbf{f}_j^k).$$

(6) for $j = 0, \ldots, J-1$, set $x_{j+\frac{1}{2}} = \frac{1}{2}(x_j + x_{j+1})$.
(7) set $n_h^{k+\frac{1}{2}}(x) \in \tilde{X}^h$ to be the piecewise linear interpolating function such that $n_h^{k+\frac{1}{2}}(x_{j+\frac{1}{2}}) = n_{j+\frac{1}{2}}^{k+\frac{1}{2}}$ for $j = 0, 1, \ldots, J-1$.
(8) solve the discretized Poisson equation on $[x_l + \frac{h}{2}, x_r - \frac{h}{2}]$ to obtain $\phi_h(n_h^{k+\frac{1}{2}})$.
(9) for $j = 0, \ldots, J-1$, set $\phi_{j+\frac{1}{2}}^{k+\frac{1}{2}} = \phi_h(n_h^{k+\frac{1}{2}})|_{x=x_{j+\frac{1}{2}}}$.
(10) for $j = 0, \ldots, J-1$, set

$$\mathbf{f}_{j+\frac{1}{2}}^{k+\frac{1}{2}} = \mathbf{f}\left(\mathbf{u}_{j+\frac{1}{2}}^{k+\frac{1}{2}}\right) = \begin{bmatrix} n_{j+\frac{1}{2}}^{k+\frac{1}{2}}\, v_{j+\frac{1}{2}}^{k+\frac{1}{2}} \\ \frac{1}{2}\left(v_{j+\frac{1}{2}}^{k+\frac{1}{2}}\right)^2 + \phi_{j+\frac{1}{2}}^{k+\frac{1}{2}} \end{bmatrix}.$$

(11) for $j = 0, \ldots, J-1$, compute $\mathbf{u}_j^{k+1}$ as

$$\mathbf{u}_j^{k+1} = \frac{1}{2}\left(\mathbf{u}_{j-\frac{1}{2}}^{k+\frac{1}{2}} + \mathbf{u}_{j+\frac{1}{2}}^{k+\frac{1}{2}}\right) + \frac{1}{2}\frac{\Delta t}{\Delta x}\left(\mathbf{f}_{j+\frac{1}{2}}^{k+\frac{1}{2}} - \mathbf{f}_{j-\frac{1}{2}}^{k+\frac{1}{2}}\right).$$

We remark that the algorithm assumes that the computational domain $I = [x_l, x_r]$ is finite and not the whole real line. It is, therefore, important to select properly the end points of this domain and the boundary conditions. For the Poisson equation, we anticipated in Sec. II B that the potential has the limit values $\phi(-\infty) = 0$ and $\phi(+\infty) = \ln(n_r)$. We choose to prescribe homogeneous Neumann boundary conditions at $x = x_l$ and $x = x_r$ and then select a large enough domain I, i.e., select x_l and x_r far enough away on each side of the origin, so that the numerical solution matches the limit values of the potential to within a small tolerance (about 10^{-4}) at the boundaries x_l and x_r of the computational domain. For all our simulations, we have confirmed that enlarging the length of the interval $I = [x_l, x_r]$ beyond what we use does not affect the numerical solutions obtained. For the velocity and ion density, we expect that the exact solutions are almost constant far from the origin, so we set $\mathbf{u}_0^k = \mathbf{u}_1^k$ and $\mathbf{u}_J^k = \mathbf{u}_{J-1}^k$ for the primal grid, and similarly for the staggered grid.

2. Lagrangian scheme for expansion into a vacuum

Consider the domain $I^t = [x_l(t), x_f(t)]$, where $x_f(t)$ denotes the position of the ion front at time t. At time $t = 0$, $I^0 = [x_l(0), 0]$ and $n(x, 0) = 1$ on I^0. The Poisson equation is solved on the extended domain $I_p^t = [x_l(t), x_r(t)]$, where $x_r(t) \geq x_f(t)$. The domains I^0 and I_p^0 are partitioned in $\hat{J}$ and J subintervals, respectively, in such a way that the subintervals of I^0 also belong to I_p^0. In order to simulate the expansion into vacuum, we need to change the boundary conditions at the boundary of the domain. In fact, in this case, $\phi \to -\infty$ as $x \to +\infty$. Therefore, it is not possible to reach the limit value of the potential in a finite domain. However, the Poisson equation can be analytically solved in (x_f, ∞), given the potential $\phi(x)$ at any $x > x_f$, x_f being the front position; see Ref. 3. We then have the boundary condition at $x_r > x_f$

$$\left.\frac{\partial\phi}{\partial x}\right|_{x_r} = -\sqrt{2}\exp\left(\frac{\phi(x_r)}{2}\right)$$

by imposing that analytical solution. As for the system (14), we use the following Lagrangian scheme for updating the velocity and the grid points:

$$v_j^{k+\frac{1}{2}} = v_j^k - \frac{1}{2}\Delta t\, \phi_{x,j}^k, \quad x_j^{k+1} = x_j^k + \Delta t\, v_j^{k+\frac{1}{2}},$$
$$v_j^{k+1} = v_j^{k+\frac{1}{2}} - \frac{1}{2}\Delta t\, \phi_{x,j}^{k+1},$$

where $\phi_{x,j}$ is defined as

$$\phi_{x,j}^k = \frac{\phi_{j+1}^k - \phi_{j-1}^k}{x_{j+1}^k - x_{j-1}^k}, \quad j = 0, \ldots, J-1$$

and

$$\phi_{x,K}^k = -\sqrt{2}\exp\left(\frac{\phi_J^k}{2}\right).$$

The mass conservation equation for ion concentrations is simply solved by

$$n_j^{k+1} = n_j^k \frac{x_{j+1}^k - x_{j-1}^k}{x_{j+1}^{k+1} - x_{j-1}^{k+1}}.$$

3. Numerical method for Vlasov–Poisson system

Several numerical methods for solving the nonlinear Vlasov equation have been proposed in the literature; see, e.g., Refs. 19–22. In this work, we use a semi-Lagrangian approach after performing a Gudunov splitting. Namely, to march from $t = t^n$ to $t = t^{n+1}$, we solve the two one-dimensional problems

$$\begin{cases} \dfrac{\partial f^*}{\partial t} + \dfrac{\partial}{\partial \mathrm{v}}\left(-\dfrac{\partial \phi}{\partial x} f^*\right) = 0 \\ f^*(t^n) = f(t^n) \end{cases} \tag{A1}$$

and

$$\begin{cases} \dfrac{\partial f}{\partial t} + \dfrac{\partial}{\partial x}(\mathrm{v} f) = 0 \\ f(t^n) = f^*(t^{n+1}). \end{cases} \tag{A2}$$

Note that both problems are scalar advection equations with constant coefficients. In particular, $\phi(x)$ is constant when solving the system (A1) from t^n to t^{n+1}; in fact, by v-integrating the equation in (A1), we have that $\frac{\partial n}{\partial t} = 0$, which implies $\phi(x)$ is constant in time. The two systems in (A1) and (A2) can be solved analytically to obtain

$$\begin{aligned} f^*(x, \mathrm{v}, t^{n+1}) &= f\left(x, \mathrm{v} + \Delta t \frac{\partial \phi}{\partial x}, t^n\right) \\ f(x, \mathrm{v}, t^{n+1}) &= f^*(x - \Delta t\, \mathrm{v}, \mathrm{v}, t^{n+1}), \end{aligned} \tag{A3}$$

respectively. We consider a rectangular domain $Q = [x_l, x_r] \times [\mathrm{v}_b, \mathrm{v}_u]$ that is large enough, so that it is reasonable to assume homogeneous Neumann condition at the inflow boundaries. The domain Q is discretized uniformly in the x and v coordinates with discretization steps Δx and $\Delta \mathrm{v}$, respectively. At each time step, f is approximated by a piecewise bilinear function with respect to the x-v grid. Function evaluations appearing in (A3) are performed using linear interpolation. In order to achieve higher-order of accuracy, instead of linear interpolation, cubic spline interpolation is often used; see, e.g., Ref. 21. However, we prefer to use linear interpolation because it guarantees that the overall method is monotone.

[1] A. Gurevich, L. Pariĭskaya, and L. Pitaevskiĭ, J. Exp. Theor. Phys. **01**(22), 449 (1966).
[2] L. Tonks and I. Langmuir, Phys. Rev. **34**, 876 (1929).
[3] J. Crow, P. Auer, and J. Allen, J. Plasma Phys. **14**, 65 (1975).
[4] E. Clark, K. Krushelnick, M. Zepf, F. Beg, M. Tatarakis *et al.*, Phys. Rev. Lett. **85**, 1654 (2000).
[5] P. Mora, Phys. Rev. Lett. **90**, 185002 (2003).
[6] T. Grismayer and P. Mora, Phys. Plasmas **13**, 032103 (2006).
[7] A. Kaplan, B. Dubetsky, and P. Shkolnikov, Phys. Rev. Lett. **91**, 143401 (2003).
[8] L. Tonks and I. Langmuir, Phys. Rev. **33**, 195 (1929).
[9] C. Mouhot and C. Villani, J. Math. Phys. **51**, 015204 (2010).
[10] J. Allen and A. Phelps, Rep. Prog. Phys. **40**, 1305 (1977).
[11] B. Fried and R. Gould, Phys. Fluids **4**, 139 (1961).
[12] J. Allen and J. Andrews, J. Plasma Phys. **4**, 187 (1970).
[13] B. Keyfitz, *in Nonlinear Theory of Generalized Functions: Proceedings of the Workshop on Nonlinear Theory of Nonlinear Functions* (CRC Press, 1997), pp. 99–111.
[14] D. Braess, *Finite Elements* (Cambridge University Press, 1997).
[15] P. Ciarlet, *The Finite Element Method for Elliptic Problems* (North-Holland Publishing Company, 1978).
[16] L. Shampine, Appl. Math. Lett. **18**, 1134 (2005).
[17] L. Shampine, Appl. Numer. Anal. Comput. Math. **2**, 346 (2005).
[18] A. Cohen, Commun. Partial Differ. Equ. **9**, 751 (1984).
[19] B. A. de Dios, J. A. Carrillo, and C.-W. Shu, Math. Models Methods Appl. Sci. **22**, 1250042 (2012).
[20] N. Crouseilles, T. Respaud, and E. Sonnendrocker, Comput. Phys. Commun. **180**, 1730 (2009).
[21] F. Filbet and E. Sonnendrocker, Comput. Phys. Commun. **150**, 247 (2003).
[22] J. Schumer and J. Holloway, J. Comput. Phys. **144**, 626 (1998).